Check for updates

ADVANCED FUNCTIONAL MATERIALS
www.afm-journal.de

Microporous, Crystalline, and Water-Processable Framework Materials of Organic Amphiphile Salts

*Louis Frentzel-Beyme, Pascal Kolodzeiski, Kai Terlinden, and Sebastian Henke**

Dedicated to Prof. Dr. Klaus Jurkschat on the occasion of his 70th birthday

Porous framework materials are of major importance for a wide range of technologies. Nevertheless, many of these materials lack processibility as they are typically synthesized under rather harsh conditions and obtained as microcrystalline powders that cannot easily be coated or deposited from solution. Herein, a new approach to water-processable metal–organic framework materials is presented. The materials are based on amphiphilic organic building blocks consisting of polar carboxylate groups and non-polar alkyl chains connected to a rigid aromatic core. The amphiphilic building blocks assemble to porous framework structures via bonding to kinetically labile sodium ions from concentrated aqueous solution. The obtained crystalline materials, termed amphiphile salt frameworks , are thermally and mechanically stable (some derivatives up to 365 °C and up to at least 4000 bar hydrostatic pressure), exhibit persistent microporous channels accessible to several gases (N_2, CO_2, propane, propylene, *n*-butane), and can be reversibly assembled/disassembled by crystallization from or dissolution in water. Systematic variation of the hydrophobic side chains of the amphiphile building blocks allows extracting structure-property relationships and first design rules for this new class of water-processable microporous framework materials.

1. Introduction

Porous solid-state materials are essential for many technological processes in today's industrial society. Their most prominent application fields are in molecular separation, purification and catalysis.[1–4] On an industrial scale, conventional inorganic porous materials, such as zeolites and activated carbons, are predominantly used as they have two big advantages: low toxicity and very low cost.[4,5] Aside these conventional application fields, porous materials are also proposed to act beneficially in several emerging technologies specialized in the energy or health sector.[6–11] The requirements for this wide range of applications, however, cannot be fully covered by the state-of-the-art of porous materials,[12,13] so that fundamental research on the development of new porous materials with tailored properties continues to be of high relevance.[6,14,15] For the precise control of the materials properties, utilization of organic building units in porous materials turned out to be particularly valuable, as the whole tableau of organic synthetic modifications can be used to implement numerous functions in the materials.[6,7,16–19]

In the past decades, academic research on porous materials containing organic building units largely focused on porous framework materials (PFMs), such as metal–organic frameworks (MOFs)[20–22] or covalent organic frameworks (COFs).[23–25] PFMs feature robust crystalline structures with well-defined pore structures.[26,27] Via the established design concept of reticular synthesis, structure and function of these materials can be tuned and tailored largely at will.[28] More recently, porous molecular materials (PMMs), such as organic cages[29–32] or metal–organic cages[33,34] (MOCs, also named coordination cages) have emerged as a viable alternative for PFMs.[6,35–42] An important conceptual advantage of PMMs is their solubility and straightforward processability from solution,[36] allowing not only for simple solution casting of thin films and mixed matrix membranes, but also for increased structural and functional complexity via cocrystal formation as well as straight forward materials recycling by repeated dissolution and crystallization.[43] The weak intramolecular interactions between the porous molecules facilitate solubility and solution processability, however, often result in limited thermal and mechanical stability.[6] Moreover, the non-directionality of the mostly dispersive intermolecular interactions between PMMs results in a loose packing of the porous molecules in the solid-state[43] frequently causing partial loss of crystallinity or even full amorphization upon removal of solvent molecules from the pores.[6,34,36]

Nevertheless, highly regular materials with well-defined pore structures are especially important as porosity features (i.e., pore size, pore volume, pore aperture size and specific surface area)

L. Frentzel-Beyme, P. Kolodzeiski, K. Terlinden, S. Henke
Anorganische Chemie
Fakultät für Chemie und Chemische Biologie
Technische Universität Dortmund
Otto-Hahn Straße 6, 44227 Dortmund, Germany
E-mail: sebastian.henke@tu-dortmund.de

The ORCID identification number(s) for the author(s) of this article can be found under https://doi.org/10.1002/adfm.202302033

© 2023 The Authors. Advanced Functional Materials published by Wiley-VCH GmbH. This is an open access article under the terms of the Creative Commons Attribution-NonCommercial License, which permits use, distribution and reproduction in any medium, provided the original work is properly cited and is not used for commercial purposes.

DOI: 10.1002/adfm.202302033

16163028, 2023, 36, Downloaded from https://advanced.onlinelibrary.wiley.com/doi/10.1002/adfm.202302033 by Technische Universitaet Dortmund, Wiley Online Library on [20/01/2025]. See the Terms and Conditions (https://onlinelibrary.wiley.com/terms-and-conditions) on Wiley Online Library for rules of use; OA articles are governed by the applicable Creative Commons License

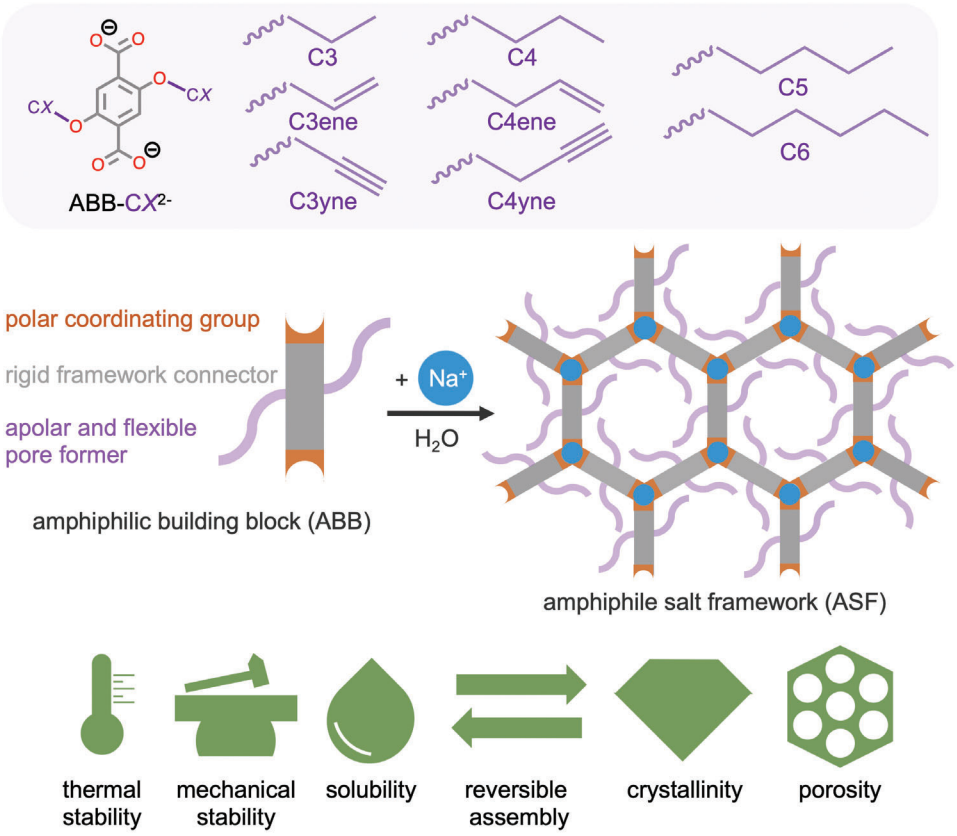

Figure 1. Top: Generalized representation of the molecular structure of an amphiphilic building block (ABB-CX^{2-}) and library of utilized pore formers. Middle: Representation of the design principle for ASFs. Bottom: Pictograms of the beneficial properties of ASFs, combining properties of PFMs and PMMs in one material class.

must be controllable for applications in gas storage/separation or molecular sieving.[13,44] Such control can be achieved in PFMs that feature directive and comparably strong coordinative or even covalent bonding between their building blocks.[8,25] This helps to obtain well-defined framework structures with precise pore sizes and high regularity[8,27] as well as high thermal[45] and mechanical[46] stability. Unfortunately, for the synthesis of such materials energy consuming solvothermal reaction routes are commonly needed.[12] Additionally, solvent molecules – which are often required to template the porous structure[47] – are interacting strongly with the framework resulting in energy-intensive activation processes (e.g., consecutive solvent exchange procedures followed by solvent removal at high temperature). Furthermore, repetitive materials recycling via disassembly and reassembly of the frameworks becomes unattractive and complex since framework dissolution is only achieved in strongly acidic or strongly basic solvent mixtures, often also requiring high temperatures.[6] Consequently, full reconstruction of the porous framework from solution requires repeated solvothermal synthesis, the presence of molecular templates as well as toxic and/or corrosive solvents.

In this work, we present a unique class of permanently porous and water-processible MOF materials, termed amphiphile salt frameworks (ASFs). ASFs combine the advantageous aspects of PFMs (rigidity, crystallinity and thermal/mechanical stability) with those of PMMs (solubility and reversible assembly) in a new class of framework solids (**Figure 1**). The ASFs are based on organic amphiphilic building blocks (ABBs) containing a polar and rigid framework connector (i.e., an aromatic dicarboxylate) as well as non-polar and flexible pore formers (saturated or unsaturated alkyl chains). Rapid assembly of these ABBs with non-toxic and low-cost sodium ions (Na^+) from aqueous solution at temperatures between 50 and 80 °C results in the formation of crystalline honeycomb-like ASFs with hydrophobic porous channels even in quantitative yields. The ASFs can be reversibly disassembled and reassembled by dissolution in water followed by crystallization during water evaporation. Stability measurements regarding high temperature and high mechanical pressure combined with elaborate gas sorption measurements demonstrate the potential of the ASFs for various application fields.

2. Results and Discussion

2.1. Design Concept of ASFs

The design concept of ASFs is inspired by the established chemistry of lyotropic liquid crystals in water, where the assembly process of the amphiphilic mesogens is based on specific attractive and repulsive interactions of the polar and non-polar parts of the amphiphiles with the solvent, leading to the aggregation of

© 2023 The Authors. Advanced Functional Materials published by Wiley-VCH GmbH

16163028, 2023, 36, Downloaded from https://advanced.onlinelibrary.wiley.com/doi/10.1002/adfm.202302033 by Technische Universitaet Dortmund, Wiley Online Library on [20/01/2025]. See the Terms and Conditions (https://onlinelibrary.wiley.com/terms-and-conditions) on Wiley Online Library for rules of use; OA articles are governed by the applicable Creative Commons License

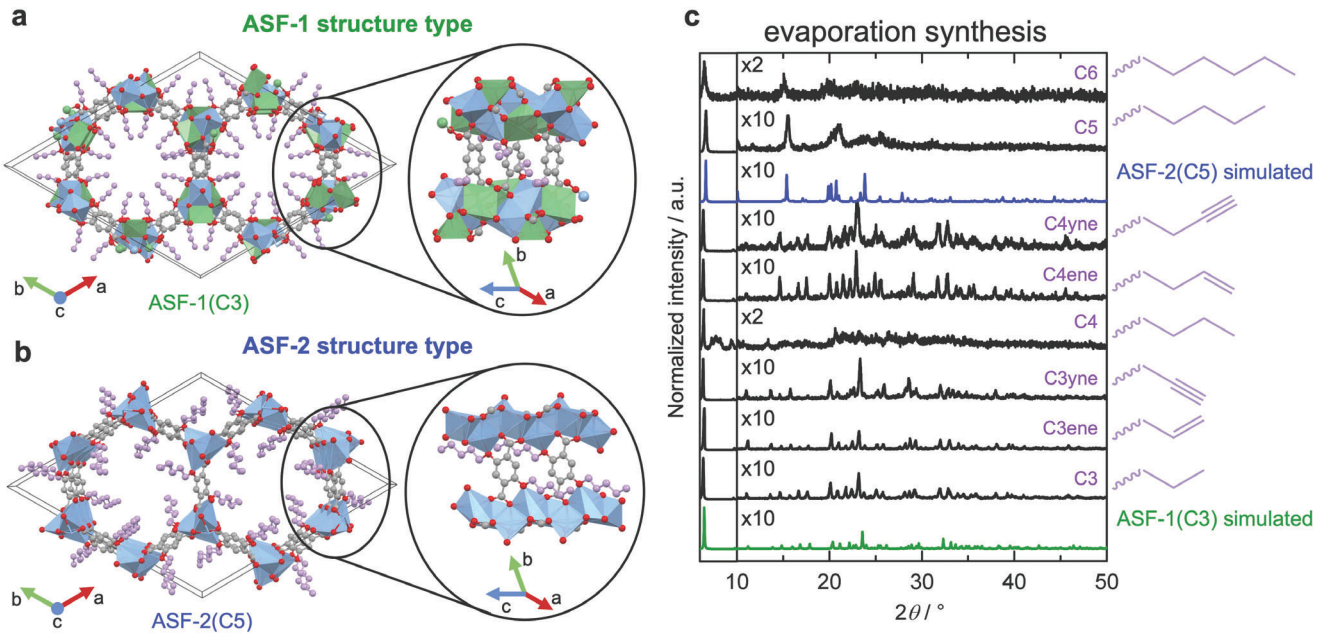

Figure 2. a) Representation of the ASF-1 structure-type exemplarily for ASF-1(C3). b) Representation of the ASF-2 structure-type exemplarily for ASF-2(C5). In panel a and b, a view along the crystallographic *c* axis visualizing the honeycomb-like structure motif is shown on the left. A view perpendicular to the crystallographic *c* axis representing the packing of the ABBs and the $[NaO_6]_n$ helices is shown on the right. Label: Na (blue/green), C (gray/purple), O (red), hydrogen atoms are omitted for clarity, coordination environments of Na^+ are shown as blue or green polyhedra. c) Stack plot of PXRD patterns obtained after the evaporation synthesis method. The pore former (C*X*) attached to the ABB applied in the synthesis is shown on the right. Simulated PXRD patterns for ASF-1(C3) and ASF-2(C5) are displayed for comparison.

the amphiphiles to micellar structures driven by the hydrophobic effect.[48–50] In order to drive the assembly of the ABBs for crystallization of honeycomb-like ASFs, the ABBs feature the following structure-directing functionalities (Figure 1):

i) A shape-persistent core (here a benzene ring) that provides the framework with rigidity and determines the metrics of the framework assembly.
ii) Two negatively charged carboxylate groups – the hydrophilic part of the ABBs – arranged in a divergent manner to facilitate formation of an extended framework by coordination to metal ions.
iii) Two non-polar and flexible alkoxy side chains – the hydrophobic part of the ABBs – which drive the micellar hexagonal assembly of the ABBs in water by the hydrophobic effect.

In concentrated aqueous solution, the anionic organic amphiphiles assemble to rod-shaped micellar structures with a hexagonal packing followed by ASF crystallization via coordination of the carboxylate groups to Na^+ cations (Figure 1). The strongly ionic Na–O bonds support a robust framework structure, while the bonds are also kinetically labile regarding hydrolyses, thus aiding a rapid assembly/disassembly of highly crystalline frameworks in water.

2.2. Synthesis

Ten 2,5-alkoxy-1,4-benzenedicarboxylic acid derivatives (H_2ABB-C*X*) were selected as ABBs and synthesized following modified literature protocols.[51,52] Their purity was verified by ^{1}H and ^{13}C nuclear magnetic resonance (NMR) spectroscopy (see Supporting Information Section S1). These H_2ABB-C*X* derivatives differ in the number of carbon atoms (C*X* = C2-C7) of the pore forming alkoxy chains (Figure 1 top). For C3 and C4 variants with terminal double (denoted C3ene and C4ene) or triple bonds (denoted C3yne and C4yne) are included.

The ASFs of the typical chemical formula Na_2(ABB-C*X*) were prepared using several different procedures (see Supporting Information S1 for further details). Slow solvothermal crystallization of the ABBs with sodium acetate was performed in a mixture of water, ethanol and *N*,*N*-dimethylformamide at 120 °C to obtain needle-shaped single crystals (sizes up to 100 µm or more) suitable for structure determination via single crystal X-ray diffraction (SCXRD). Microcrystalline powders were obtained by dissolution of the ABBs in aqueous sodium hydroxide solution followed by evaporation of the water under reduced pressure at 80 °C using a rotary evaporator (evap-a) or from an open vessel at 50 °C in an oven (evap-b).

2.3. Structural Characterization

The crystal structures of the ASFs were determined by SCXRD using crystals derived by solvothermal synthesis (**Figure 2**a,b). The ASFs with C*X* = C3, C3ene, C3yne, C4, C4ene, C4yne, C5 and C6 are crystallizing in 3D honeycomb-like microporous frameworks with trigonal space groups ($R\bar{3}$; $R\bar{3}c$, $P3_1$). The frameworks exhibit the general chemical composition Na_2(ABB-C*X*), except for ABB-C6^{2-} which yields a material of the composition

© 2023 The Authors. Advanced Functional Materials published by Wiley-VCH GmbH

16163028, 2023, 36, Downloaded from https://advanced.onlinelibrary.wiley.com/doi/10.1002/adfm.202302033 by Technische Universitaet Dortmund, Wiley Online Library on [20/01/2025]. See the Terms and Conditions (https://onlinelibrary.wiley.com/terms-and-conditions) on Wiley Online Library for rules of use; OA articles are governed by the applicable Creative Commons License

Table 1. Data representing the differences in porosity of ASFs. The evaluation has been performed based on the structural models obtained by SCXRD (see Supporting Information S6 for details). The "largest included sphere" represents the largest size of a sphere that can be hosted in the pores of the framework, while the "largest free sphere" represents the size of the largest sphere that can freely diffuse through the pores.

	ABB density/ ABBs nm^{-3}	tVF/%	Diameter (largest included sphere)/Å	Diameter (largest free sphere)/Å
ASF-1(C3)	2.58	9	5.49	4.80
ASF-1(C3ene)	2.54	22	7.24	6.68
ASF-1(C3yne)	2.58	17	6.48	5.99
ASF-2(C4)	2.18	10	5.32	4.63
ASF-1(C4ene)	2.54	4	3.77	3.31
ASF-1(C4yne)	2.56	6	4.43	4.02
ASF-2(C5)	1.85	13	5.68	4.79
ASF-2(C6)	1.83	2	2.75	2.10

Na_2(ABB-C6)$(H_2O)_{0.5}$. Depending on the length and flexibility of the respective pore former, we find two different honeycomb-like structure types denoted ASF-1(C*X*) (for C*X* = C3, C3ene, C3yne, C4, C4ene, C4yne) and ASF-2(C*X*) (for C*X* = C4, C5, C6). Notice that ABB-C4 forms a phase mixture of both ASF structure types, which we will discuss in more detail below. The framework formation is driven by a micellar aggregation of the amphiphilic building blocks controlled by their hydrophobic alkyl chains (pore formers) which are lining the porous channels of the honeycomb-like structure motifs. Accordingly, the structure of these ASFs is akin to micellar hexagonal phases of lyotropic liquid crystals and hydrogen bonded dipeptides,[48–50] however, the framework structures of the ASFs are characterized by strong ionic bonding between the polar carboxylate groups of the ABBs and Na^+ ions.

In the ASF-1 structure-type an off-centered parallel stacking of the benzene rings of adjacent ABBs with a plane-plane distance of 3.27 Å is found, indicating that attractive π–π-interactions between neighboring benzene rings stabilize this structure motif with the shorter pore formers (Figure 2a).[53,54] On the contrary, in the ASF-2 structure-type a large offset of adjacent ABB benzene rings is found, resulting from the more sterically demanding pore formers (ABB-C5^{2-} and ABB-C6^{2-}) and preventing favorable π–π-stacking (Figure 2b). Consequently, shorter alkyl groups (ASF-1 structure type) allow a denser packing of the amphiphilic building units (ASF-1C*X*) 2.54 – 2.58 ABBs nm^{-3}; ASF-2(C*X*) minimum 1.83 – 2.18 ABBs nm^{-3}; **Table 1**) which overall results on a higher crystallographic density of the ASF-1 materials ($\rho \approx$ 1.28 – 1.48 g cm^{-3}) compared to the ASF-2 materials ($\rho \approx$ 1.17 – 1.28 g cm^{-3}).

The rigid part of the ABBs (framework connector) forms the edges of the honeycombs (Figure 2a,b). Based on this arrangement the carboxylate groups are clustering around the vertices of the honeycomb where they are coordinating to Na^+ ions. The Na^+ ions are six-fold coordinated by O atoms from the ABBs forming helical chains of corner-sharing [NaO_6] coordination polyhedra running parallel to the crystallographic *c* axes. As a result of the denser packing of the ABBs in ASF-1 the $[NaO_6]_n$ helix is decorated by surrounding Na^+ ions (highlighted with green polyhedra in Figure 2a). The hydrophobic alkyl chains point inside the 1D channels driving the assembly to the honeycomb-like structure motif. Depending on the length of the alkyl chains the pore shape and surface as well as overall void fraction of the ASFs drastically varies. The theoretical void fraction (tVF) evaluated from SCXRD data is only 2% for ASF-2(C6) but increases to 22% for ASF-1(C3ene) (Table 1). The unsaturated terminal bonds (double or triple) of some pore formers influence their flexibility and conformation, resulting in different pore shapes/geometries as well as surface polarizabilities (Table 1; Figure S38, Supporting Information). We note that the porosity parameters have been calculated based on the SCXRD data recorded at 100 K. Due to the flexible nature of the alkoxy side chains, the porosity parameters may vary at higher temperatures, particularly for the ASFs with the longer side chains.

Only a rather small residual electron density is observed in the open hydrophobic voids of the more porous ASFs, even though the crystals were directly picked from the mother liquor for the SCXRD experiments (Table S2, Supporting Information). Remarkably, the most porous derivative ASF-1(C3ene) features only a tiny residual electron density of about 1.7 e^- per ASF formula unit. This signifies that the pores of ASF-1(C3ene) are readily guest-free after synthesis. These observations indicate that solvent-templating does not play a significant role for the crystallization of the honeycomb-like porous ASF structures.

Powder X-ray diffraction (PXRD) experiments verify that all solvothermally synthesized ASFs are phase pure apart from the sample derived from H_2ABB-C4 (Figures S2–S9, Supporting Information). Here, a phase mixture of the ASF-1 and ASF-2 structure-type is found, verified by a dual-phase profile fit of the PXRD pattern (Figure S5, Supporting Information). Unfortunately, by selecting several single crystals from the reaction mixture only crystals of the ASF-1 structure-type were found in SCXRD experiments. Remarkably, utilizing H_2ABB-4ene and H_2ABB-4yne in the solvothermal synthesis yielded phase pure materials of the ASF-1 structure type. Here, the impact of the length and the flexibility of the pore former on the derived ASF structure-type becomes further evident. The steric demand and flexibility of the C4 side chain of ABB-C4^{2-} appear to define the region where both ASF structure-types are energetically similar, so that the ASF-1(C4) and ASF-2(C4) phases form in parallel.

We note that a short chain of only two carbon atoms in the pore former (H_2ABB-C2), generates an ASF-3(C2) material featuring a densely packed crystal structure with a rhombic arrangement of the building units in a triclinic lattice (space group $P\bar{1}$), leaving the material overall non-porous (see Supporting Information S10 for a detailed structural description). A change from a hexagonal to a rhombic arrangement of building units by shortening the length of the structure directing side chains has been previously observed for liquid crystal formation in the literature.[50] Sodium 1,4-benzenedicarboxylate (terephthalate), which represents the corresponding material without any side chains (pore formers) attached to the benzene core, was previously reported to crystallize in a non-porous layered structure,[55] highlighting the effect of the side chains on ASF assembly. An increase of the chain lengths to seven carbon atoms (H_2ABB-C7) led to a microcrystalline powder with a diffraction pattern that does neither match to ASF-1 nor the ASF-2 structure type (Figure S10, Supporting Information). Given that the pore space available in the ASF-2(C6) is already very small (tVF = 2%), the bulk of the

 © 2023 The Authors. Advanced Functional Materials published by Wiley-VCH GmbH

16163028, 2023, 36, Downloaded from https://advanced.onlinelibrary.wiley.com/doi/10.1002/adfm.202302033 by Technische Universitaet Dortmund, Wiley Online Library on [20/01/2025]. See the Terms and Conditions (https://onlinelibrary.wiley.com/terms-and-conditions) on Wiley Online Library for rules of use; OA articles are governed by the applicable Creative Commons License

C7 chain is too large to support the formation of a honeycomb-like ASF structure. Unfortunately, several attempts to grow single crystals of Na_2(ABB-C7) large enough for SCXRD remained unsuccessful, so that the structure of this material cannot yet be resolved.

2.4. Rapid Crystallization of ASFs from Water

As already indicated by the very low amount of solvent guest molecules in the pores of the ASFs observed by SCXRD, the ASFs can also be rapidly crystallized from an aqueous solution of a chosen H_2ABB-C*X* derivative and sodium hydroxide. Polycrystalline ASF powders were obtained in about 10–20 min by evaporating the water to dryness on a rotary evaporator at 80 °C (evap-a; see Supporting Information S1). Profile fits to PXRD data of the derived microcrystalline powders demonstrate the formation of phase pure ASFs except for Na_2(ABB-C4) (Figure 2c; Figures S12–S19, Supporting Information). The PXRD patterns of the ASF-2 materials prepared via the evap-a method feature broader reflections and a lower signal-to-noise ratio, which is ascribed to the higher flexibility of the longer alkoxy side chains leading to increased diffuse scattering. The ASFs prepared by the evaporation synthesis are already guest- and solvent-free as confirmed by FTIR spectroscopy showing no vibrational bands assigned to residual water molecules (Figure S32, Supporting Information). We conclude that the hydrophobic nature of the pores expels the water which yields readily porous materials under the applied crystallization conditions (80 °C, < 20 mbar).

Further, SEM images were collected of ASFs obtained after the solvothermal or evaporation synthesis approach (Figures S47–S50, Supporting Information). Most of the crystallites obtained via solvothermal synthesis appear as rod-shaped crystals of about 10 µm in length. In comparison, the ASFs generated by evaporation of water feature particles of not-so-well-defined morphologies and smaller sizes (≈1–7 µm). This observation is ascribed to the much faster crystallization process (evap-a: ≈10–20 min; solvothermal: 24 h).

Based on the kinetically labile mainly electrostatic sodium oxygen interactions it is possible to repeat the dissolution and recrystallization of ASFs from water for several times. As a proof of concept, ASF-1(C3ene) was completely dissolved in water (200 mg ASF-1(C3ene) in ≈2 mL water) and crystallized again by evaporating the water at 80 °C for ten times. FTIR spectroscopy (Figure S37, Supporting Information) and PXRD (Figures S25 and S26, Supporting Information) data prove the repeated formation of pure ASF-1(3ene). This simple water dissolution and evaporation process consequently allows processing of ASFs in aqueous solution. Generally, only very small amounts of water are necessary to completely dissolve the ASFs (molar solubilities determined at 25 °C: 0.41 mol L^{-1} for ASF-1(C3), 1.06 mol L^{-1} for ASF-1(C3ene), 0.65 mol L^{-1} for ASF-2(C5)).

2.5. Gas Adsorption Studies

We chose ASF-1(C*X*) (C*X* = C3, C3ene, C3yne) and ASF-2(C5) for gas physisorption experiments, as these are the most porous ASFs regarding their tVF (**Figure 3**a). To define a reference point for the materials rapidly precipitated from water, we first discuss the gas sorption properties of the highly crystalline and phase pure solvothermally synthesized materials. Increasing maximum gas adsorption capacities are found in the order ASF-1(C3) < ASF-2(C5) < ASF-1(C3ene) for N_2 at 77 K and CO_2 at 195 K, which is in the same order as expected from the calculated tVFs (Figure 3b,c and Table 1). Remarkably, ASF-1(C3yne) shows by far the lowest uptake for N_2 but the highest for CO_2 of all investigated ASFs. We ascribe the rather low N_2 uptake of ASF-1(C3yne) to reduced conformational flexibility of the terminal alkyne groups pointing into the cylindrical pores of the material. Consequently, the diffusion of N_2 (kinetic diameter 3.64 Å[56]) into the framework is restricted at 77 K. The diffusion of CO_2 (kinetic diameter 3.30 Å[56]) into the framework at higher temperature (195 K) is favored and additional attractive interactions between CO_2 and the polarizable C–C-triple bonds result in the highest CO_2 uptake amongst the series. Consequently, the Brunauer–Emmett–Teller (BET) areas (S_{BET}) calculated from the N_2 and CO_2 gas sorption isotherms of ASF-1(C3yne) differ by an order of magnitude, with S_{BET} = 34 m^2 g^{-1} for N_2 and S_{BET} = 410 m^2 g^{-1} for CO_2. Similarly, the corresponding pore volumes (V_{pore}) of the ASFs depend strongly on the utilized probe gas (**Table 2**; see Supporting Information S6 for further details).

We also collected CO_2 physisorption isotherms (195 K) of the ASFs derived by the evaporation synthesis routes (Figure 3d). Here, we found decreased maximum capacities compared to the solvothermally synthesized materials except for ASF-1(C3), which is the least porous ASF of the series. We assign the lower gas capacities of the other ASF derivatives prepared via the evap-a route to a larger number of defects in the materials obtained via the fast crystallization process. Defects may lead to a partial blocking of pores and thus lower the gas accessible volume within the materials. This is supported by N_2 gas sorption isotherms collected at 77 K for the ASFs prepared by the evap-a method, which all show a flat rise of the isotherm with pressure indicating predominant adsorption on the outer particle surfaces and micropores blocked for N_2 at 77 K (see Figure S40, Supporting Information).

We attempted to reduce the number of such defects and increase the gas sorption capacity by slowing down the crystallization process from aqueous solution via decreasing the reaction temperature from 80 to 50 °C and performing the reaction without reduced pressure (evap-b; see Supporting Information S1). Indeed, we found an increase of CO_2 adsorption capacity for ASF-1(C3ene) (+8% with respect to the materials prepared via evap-a) and ASF-2(C5) (+23% compared to the material prepared via evap-a) (Tables S17–S19, Supporting Information). Unfortunately, ASF-1(C3yne) yields a phase mixture of the ASF-1 structure-type and a non-porous hydrate phase of the composition $[Na_2(H_2O)_6]$[ABB-3yne] by conducting the slow crystallization process at 50 °C (Figure S22 and Supporting Information S11). The derived phase mixture of ASF-1(C3yne) and its hydrate was not further investigated by gas adsorption studies.

The largest difference in CO_2 capacity between the material obtained by the evap-a route and the one prepared via solvothermal synthesis is found for ASF-2(C5) (−47% at 95 kPa and 195 K). Profile fits to PXRD data display a 7% smaller unit cell volume for the material prepared by the water evaporation methods (evap-a and evap-b) compared to the ASF-2(C5) derived via

© 2023 The Authors. Advanced Functional Materials published by Wiley-VCH GmbH

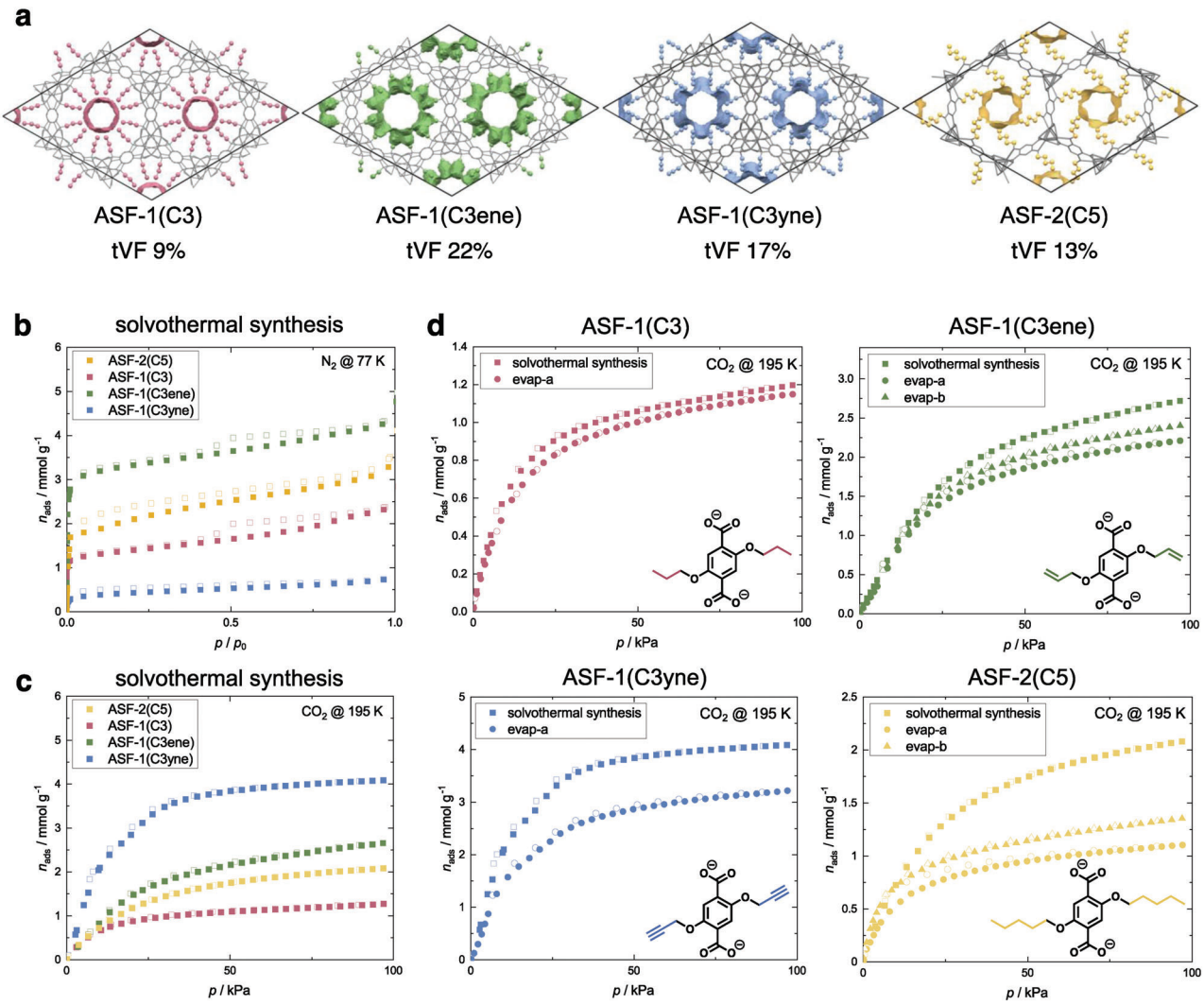

Figure 3. a) Representation of the crystal structures of selected ASFs investigated via gas physisorption experiments. All atoms are colored gray (style: wireframe) except for the pore formers highlighted in different colors (style: ball and stick). H atoms are omitted. The given calculated void fractions are highlighted (grid spacing 0.2 Å probe radius 1.2 Å). b,c) N_2 sorption isotherms recorded at 77 K (b) and CO_2 sorption isotherms recorded at 195 K (c) for ASFs obtained by the solvothermal synthesis route. d) CO_2 sorption isotherms collected at 195 K for the ASFs prepared by different synthesis routes. The respective ABB present in the ASF is displayed on the bottom right of each graph. In panel (b), (c) and (d), adsorption and desorption branches are shown as closed and open symbols, respectively.

Table 2. Summary of BET areas (S_{BET}) and pore volumes (V_{pore}) determined from N_2 isotherms recorded at 77 K and CO_2 isotherms recorded at 195 K.

	N_2 @ 77 K		CO_2 @ 195 K	
	S_{BET}/m^2 g^{-1}	V_{pore}/cm^3 g^{-1}	S_{BET}/m^2 g^{-1}	V_{pore}/cm^3 g^{-1}
ASF-1(C3)	115	0.08	106	0.04
ASF-1(C3ene)	294	0.15	282	0.10
ASF-1(C3yne)	34	0.03	410	0.14
ASF-2(C5)	209	0.11	191	0.07

solvothermal synthesis (Tables S10–S12, Supporting Information). We assume that a closer packing of the less dense ASF-2(C5) material (ρ_{calc} = 1.175 g cm^{-3}) is possible due to contraction of the single $[NaO_6]_n$ helices in the ASF-2 structure type. This is supported by FTIR spectroscopy data of ASF-2(C5) materials obtained after the solvothermal and evaporation synthesis route which uncover the occurrence of additional vibrational bands at about 1400 cm^{-1} and shifting of the band at ≈1600 cm^{-1} (Figure S33, Supporting Information). Since these bands are assigned to the symmetric (around 1400 cm^{-1}) and asymmetric (around 1600 cm^{-1}) carboxylate stretching modes, it is implied that different coordination modes of the carboxylates to Na^+ ions are present in ASF-2(C5) prepared via evaporation synthesis. We hypothesize that these differences arise from distortions of the $[NaO_6]_n$ helices or even defects (e.g., a wrongly coordinating linker), which partially block the pores.

Similar defects might also be the reason for the lower gas capacities of some rapidly precipitated ASF-1(C*X*) derivatives (C*X* = C3ene, C3yne) (Figure 3d). However, neither a change in the

© 2023 The Authors. Advanced Functional Materials published by Wiley-VCH GmbH

16163028, 2023, 36, Downloaded from https://advanced.onlinelibrary.wiley.com/doi/10.1002/adfm.202302033 by Technische Universitaet Dortmund, Wiley Online Library on [20/01/2025]. See the Terms and Conditions (https://onlinelibrary.wiley.com/terms-and-conditions) on Wiley Online Library for rules of use; OA articles are governed by the applicable Creative Commons License

16163028, 2023, 36, Downloaded from https://advanced.onlinelibrary.wiley.com/doi/10.1002/adfm.202302033 by Technische Universitaet Dortmund, Wiley Online Library on [20/01/2025]. See the Terms and Conditions (https://onlinelibrary.wiley.com/terms-and-conditions) on Wiley Online Library for rules of use; OA articles are governed by the applicable Creative Commons License

FTIR spectra nor a significantly reduced unit cell volume is observed for any of the ASF-1 materials prepared via evaporation synthesis (Figures S34–S36 and Tables S9, S11, S12, Supporting Information). A reason for that could be, that adjacent ABBs in the ASF-1 structure-type feature additional π–π-interactions which help directing the formation of this frameworks. Hence, less defects arise even if the materials are crystallized rapidly from water. Moreover, the $[NaO_6]_n$ helices in the ASF-1 materials are additionally decorated with Na^+ ions yielding a higher connectivity of the rod-shaped inorganic building unit compared to the undecorated $[NaO_6]_n$ helices in the ASF-2 materials.

Remarkably, the typical Langmuir-shape of all CO_2 isotherms of the ASFs features a rather flat rise at low pressure – less pronounced for ASF-1(C3yne) – as a signature for the apolar nature of the pore surfaces. Thus, we moved on and tested the adsorption of several apolar hydrocarbon gases at 273 K. We again collected physisorption isotherms for materials obtained by the solvothermal synthesis route and the two different evaporation synthesis routes (**Figure 4**). Importantly, for all the hydrocarbon gases, the differences between the maximum adsorption capacities of the materials derived via the solvothermal and evaporation synthesis routes are much less pronounced (**Figure 5**). We ascribe this to attractive interactions between the hydrophobic gas molecules and the hydrophobic pore surfaces. Remarkably, all hydrocarbon sorption isotherms for the slower crystallized ASFs (evap-b route) not only display increased capacities but also the disappearance of priory existing hysteresis, thus pointing towards a better accessibility of the pore space. For ASF-1(C3) and ASF-1(C3yne) the faster crystallized samples (evap-a route) yield nearly the same hydrocarbon sorption capacities as the solvothermal method. Additionally, almost all *n*-butane sorption isotherms of the ASF samples prepared by water evaporation show a steep rise starting above 75 kPa. This is a sign for *n*-butane condensation between the ASF particles (on the external surface) in agreement with the much smaller particle sizes of these materials as evident from SEM imaging (Figures S47–S50, Supporting Information).

Based on the various gas sorption isotherms the propylene/propane selectivity factor S_{IAST} was calculated for the ASFs under study here according to ideal adsorbed solution theory (IAST, Supporting Information S6). Even though ASF-1(C3), ASF-1(C3ene) and ASF-2(C5) feature very similar uptakes of propylene and propane at 95 kPa, propane is adsorbed preferentially as demonstrated by selectivity factors between 0.63 and 0.76 (for equimolar mixtures of propylene and propane). Remarkably, ASF-1(C3yne), exhibiting pores lined by terminal alkynyl groups, features a preference for the adsorption of propylene over propane, with a selectivity factor of 1.82 (again for equimolar mixtures of propylene and propane). The higher selectivity of ASF-1(C3yne) for propylene is ascribed to attractive interactions between the unsaturated pore former (the propargyl groups lining the pores) and the unsaturated gas molecule. Similar approaches for tuning gas sorption properties by taking advantage of designable pore shapes with saturated and unsaturated bonds rather than only single functional groups on the pore surfaces were recently also reported for PFMs.[57] The results of the IAST calculations demonstrate that the functional sorption properties of the ASFs can be modified by the choice of the pore lining side chains, thus offering potential for targeted adjustment according to the principles of reticular chemistry.

2.6. Alternative Synthesis Routes

The possibility of direct crystallization of the porous ASFs from aqueous solution is further demonstrated by drop-casting them on a glass plate. To demonstrate this, a drop of an aqueous solution of Na_2ABB-C*X* (*X* = 3, 3en, 3yne, 5) was placed on a preheated glass plate, which was then heated to 100 °C in an oven to form a solid film within about 10 min (Supporting Information S1). The phase pure formation of the respective crystalline ASF was verified by PXRD collected directly from the microcrystalline ASF film on the glass plate (Figure S24, Supporting Information).

Moreover, the self-templating nature of the porous ASFs allows their crystallization in a solvent-free mechanochemical synthesis (Supporting Information S8). Manual grinding of H_2ABB-C5 and solid NaOH in a 1:2 molar ratio using a laboratory mortar leads to the phase pure formation of ASF-2(C5) (Figure S52, Supporting Information). Performing this manual grinding approach also results in the formation of ASF-1 materials when grinding either H_2ABB-C3, H_2ABB-C3ene or H_2ABB-C3yne with NaOH (again 1:2 molar ratio; Figure S51, Supporting Information). Nevertheless, for the ASF-1(CX) materials the chemical reaction is incomplete, as visualized by reflections from impurities in the PXRD patterns of the obtained powders. This was improved by conducting the synthesis in an automatic ball mill exemplarily with H_2ABB-3ene and NaOH which helped to enhance the conversion to ASF-1(C3ene) by 5 min ball milling (Figure S54, Supporting Information). Gas accessible porosity of the mechanochemically synthesized ASF was further confirmed by CO_2 gas sorption analysis (see Figure S41, Supporting Information). In general, it is remarkable that no additional solvent is necessary for the mechanochemical crystallization of the ASFs. Compared to conventional mechanochemical synthesis methods for MOFs, which typically require the presence of small amounts of organic solvents (e.g., DMF),[58] the water generated in situ by the neutralization reaction of H_2ABB-C*X* and NaOH is sufficient to support the crystallization of the porous framework materials. In line with the previous findings, it is also possible to recrystallize the mechanochemically synthesized ASF-1(C3ene) by dissolution in water followed by water evaporation according to the evap-a method (see Figure S27, Supporting Information).

2.7. Thermal, Mechanical, and Chemical stability

The thermal stability of the ASFs was evaluated by simultaneous thermogravimetric analysis and differential scanning calorimetry (TGA/DSC, Supporting Information S4) under Ar atmosphere. ASFs carrying aliphatic alkyl chains are thermally stable to about 365 °C, indicated by no mass-loss up to this temperature and a rapid mass-loss at higher temperatures (Figure S28, Supporting Information). Lower decomposition temperatures between 260 and 290 °C are apparent for the ASFs carrying unsaturated side chains, suggesting that the thermal sensitivity of the pore formers is the reason for their lower thermal stability (Figures S29 and S30, Supporting Information).

© 2023 The Authors. Advanced Functional Materials published by Wiley-VCH GmbH

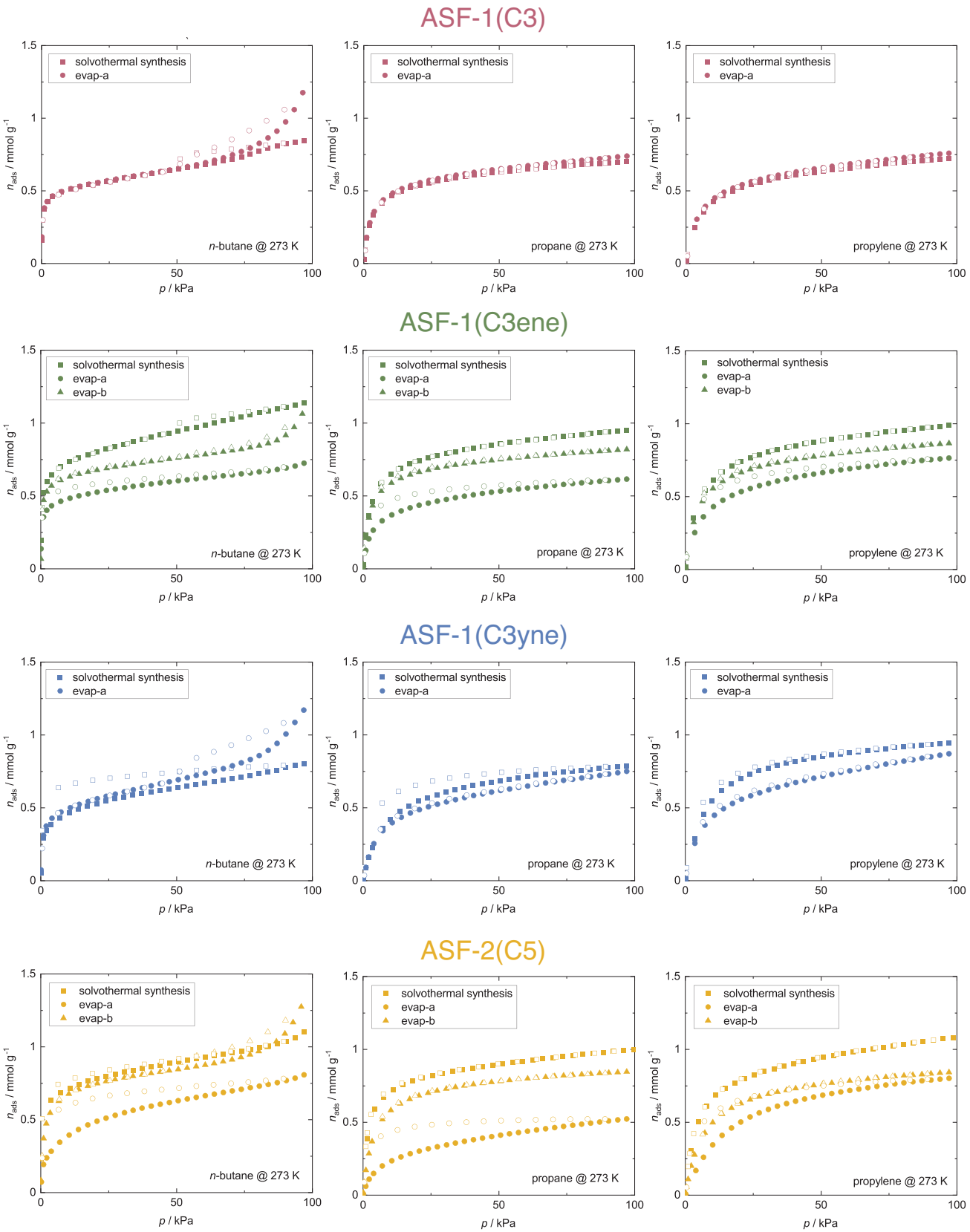

Figure 4. Hydrocarbon physisorption isotherms collected at 273 K for several ASF materials prepared via the different synthesis routes. Adsorption and desorption branches are shown as closed and open symbols, respectively.

© 2023 The Authors. Advanced Functional Materials published by Wiley-VCH GmbH

16163028, 2023, 36, Downloaded from https://advanced.onlinelibrary.wiley.com/doi/10.1002/adfm.202302033 by Technische Universitaet Dortmund, Wiley Online Library on [20/01/2025]. See the Terms and Conditions (https://onlinelibrary.wiley.com/terms-and-conditions) on Wiley Online Library for rules of use; OA articles are governed by the applicable Creative Commons License

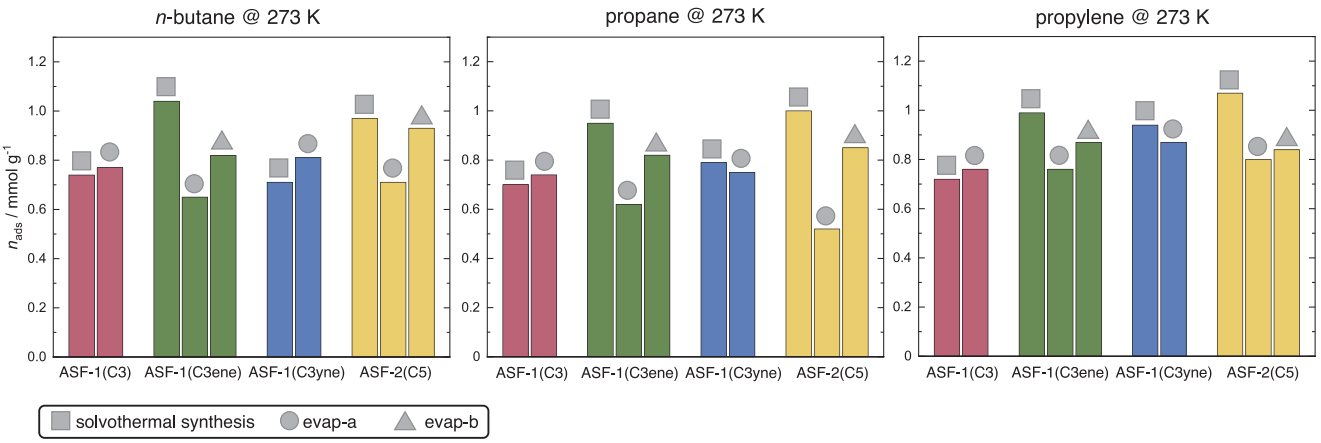

Figure 5. Graphs comparing the maximum gas capacities of several hydrocarbon gases at 75 kPa (*n*-butane) or 95 kPa (propane and propylene) and 273 K for the ASFs obtained via the solvothermal and evaporation synthesis routes. For *n*-butane a pressure of 75 kPa was used to exclude effects of inter-particle condensation.

The mechanical stability was investigated by in situ high pressure PXRD for ASF-1(C*X*) with $X = 3$, 3ene, 3yne and ASF-2(C5) performed with synchrotron radiation (DELTA, Dortmund) at hydrostatic pressures from ambient to 3750 or 4000 bar (limited by the tightness of the hydraulic pressure cell, Supporting Information S9). The ASF-1(C*X*) materials show neither decomposition nor framework collapse when compressed up to the maximum pressures achievable with the utilized setup (3750 bar for ASF-1(C3) and ASF-1(C3ene), 4000 bar for ASF-1(C3yne)). A fully reversible linear contraction of the unit cell volume by about 3% is found for all ASF-1(C*X*) materials in the investigated pressure range. The compression mainly occurs along the crystallographic *c* axis which corresponds to a contraction of the Na^+ helices. Bulk moduli (K_0) derived via fitting the *V-p*-data to a 2nd order Birch-Murnaghan equation of state amount to 13.5(±0.2) GPa (for ASF-1(C3)), 12.9(±0.2) GPa (for ASF-1(C3yne)) and 11.4(±0.1) GPa (for ASF-1(C3ene)). These bulk moduli are comparable to the bulk moduli determined for typical transition-metal-based MOFs.[59]

In contrast, the unit cell volume of ASF-2(C5) decreases by about 13% over the investigated pressure range, with a drastic decrease of about 10% between 1000 – 2500 bar, along with the strong shifts of several Bragg reflections especially in the region from 5° – 9° 2θ (Figures S69 and S70, Supporting Information). This points towards a phase transition of ASF-2(C5) triggered by the applied mechanical pressure. Unfortunately, the high pressure PXRD data are of insufficient quality to allow for structure refinement, however, profile fitting suggests a preservation of symmetry (space group $R\bar{3}$) but a contraction of all unit cell axes. We postulate that an irreversible phase transition takes place from the ambient pressure ASF-2(C5) phase to a denser high pressure ASF-2(C5). In accordance with this interpretation, the unit cell volume of the compressed phase at ambient conditions (i.e., after complete pressure release from 3750 to 1 bar) is about 7% smaller (4622(2) Å^3) than the unit cell volume of the initial ASF-2(C5) phase at the start of the experiment (4954(4) Å^3). The bulk modulus of ASF-2(C5), calculated using the *V-p* data from ambient pressure to 1000 bar (i.e., before the start of the phase transition), amounts to 8.2(±0.2) GPa and is about 30% smaller than the ones of the ASF-1(C*X*) materials. This observation underlines the higher stiffness of the ASF-1 structure type, which is associated with their slightly larger densities and the higher robustness of their rod-shaped inorganic building units (i.e., the $[NaO_6]_n$ helices decorated with further Na^+ ions) exhibiting a higher connectivity.

In addition, the chemical stability of three representative ASF materials (ASF-1(C3), ASF-1(C3ene), ASF-2(C5)) was evaluated by storing each of these materials in four different organic solvents (DMF, DMSO, THF, or EtOH) for 24 h. PXRD and IR analysis collected before and after storing these materials in these solvent are virtually identical, highlighting the structural durability of all ASFs in these solvents (see Figures S76–S81, Supporting Information).

3. Conclusions

We demonstrate that the assembly of the dicarboxylate-based ABBs with Na^+ ions leads to the crystallization of a series of ASF materials exhibiting honeycomb-like networks with cylindrical channels. The packing structure of these ASFs is akin to micellar hexagonal phases of lyotropic liquid crystals and hydrogen bonded dipeptides,[48–50] while the derived frameworks are based on strong ionic bonds between anionic carboxylate groups and Na^+ cations. Depending on the length and flexibility of the chosen pore former (C*X*), we found two different honeycomb-like framework types: ASF-1(C*X*) (C*X* = C3, C3ene, C3yne, C4, C4ene, C4yne) and ASF-2(C*X*) (C*X* = C4, C5, C6).

The pore size and functionality of the ASFs can be tuned via choice of the pore former length and degree of saturation of the pore forming alkyl side chains. Gas sorption studies demonstrate permanent porosity towards various gases (N_2, CO_2, *n*-butane, propane and propylene) as well as tuneable sorption selectivity regarding the industrially relevant propylene/propane separation process. The strong but non-directional ionic bonding between the carboxylate groups of the ABBs and Na^+ ions, results in high thermal and mechanical stability (up to about 365°C and 4000 bar). At the same time, the kinetic lability of these bonds allows for reversible disassembly (dissolution) and reassembly

© 2023 The Authors. Advanced Functional Materials published by Wiley-VCH GmbH

16163028, 2023, 36, Downloaded from https://advanced.onlinelibrary.wiley.com/doi/10.1002/adfm.202302033 by Technische Universitaet Dortmund, Wiley Online Library on [20/01/2025]. See the Terms and Conditions (https://onlinelibrary.wiley.com/terms-and-conditions) on Wiley Online Library for rules of use; OA articles are governed by the applicable Creative Commons License

(recrystallization) of the ASFs in water. The corresponding repeatable liquid phase processing ability of the ASFs from the greenest solvent available (water) has so far not been demonstrated for any other class of porous framework materials.[60–62]

This unique processing property conceptually allows a simple regeneration of the materials by dissolving in water followed by recrystallization of fresh material – overcoming, e.g., materials aging issues. On that account, the ASFs can be directly deposited on surfaces by facile drop-casting from aqueous solution. Remarkably, due to the self-templating of the porous channels by micellar aggregation of the pore formers, the materials are readily porous after crystallization from water, but can also be prepared by solid-state mechanochemical synthesis without any additional solvent.

We propose that the ASF design concept demonstrated here for 2,5-dialkoxy-1,4-benzenedicarboxylate ABBs and Na^+ cations is transferable to other anionic ABBs in combination with various kinetically labile metal cations (e.g., other alkali metal ions). Future work may demonstrate that the concepts of (iso)reticular synthesis and multivariate chemistry (i.e., solid solution chemistry), both well-established for MOFs, are transferable to the new class of ASFs. We imagine that ABBs with an elongated framework connector result in isoreticular expanded ASFs with largely increased porosity. Consequently, the presented ASFs represent only the beginning for the development of a new class of water-processable porous materials merging beneficial properties of porous molecular and porous framework materials alike.

Supporting Information

Supporting Information is available from the Wiley Online Library or from the author.

Acknowledgements

This project received funding from the Deutsche Forschungsgemeinschaft (DFG) within the Priority Programme SPP1928 COORNETs (Start-Up Grand for S.H. and Gateway Fellowship for L.F.-B.) and project 415553115 (HE7628/3-1). P.K. acknowledges the Fonds der Chemischen Industrie (FCI) for a Kekulé Fellowship. Volker Brandt is acknowledged for collection of SEM images. The authors further thank the Dortmunder ELekTronenspeicherring-Anlage (DELTA) for allocation of beamtime and the BL9 staff (Michael Paulus and Christian Sternemann) for their great support with the high-pressure powder X-ray diffraction experiments.

Open access funding enabled and organized by Projekt DEAL.

Conflict of Interest

The authors declare no conflict of interest.

Author Contributions

S.H. designed the project. L.F.-B. synthesized the materials. L.F.-B., P.K. and K.T. collected and analyzed all analytical data. L.F-B. and S.H. wrote the paper.

Data Availability Statement

The data that support the findings of this study are available in the supplementary material of this article.

Keywords

amphiphile assembly, gas sorption, high-pressure crystallography, mechanochemistry, metal–organic frameworks, porosity

Received: February 21, 2023
Revised: April 24, 2023
Published online: May 18, 2023

[1] C. Martínez, A. Corma, *Coord. Chem. Rev.* **2011**, *255*, 6058.
[2] D. M. D'Alessandro, B. Smit, J. R. Long, *Angew. Chem., Int. Ed.* **2010**, *49*, 6058.
[3] C. Liang, Z. Li, S. Dai, *Angew. Chem., Int. Ed.* **2008**, *47*, 3696.
[4] B. Yilmaz, U. Müller, *Top. Catal.* **2009**, *52*, 888.
[5] W. Vermeiren, J. P. Gilson, *Top. Catal.* **2009**, *52*, 1131.
[6] A. G. Slater, A. I. Cooper, *Science* **2015**, *348*, aaa8075.
[7] B. Li, H.-M. Wen, Y. Cui, W. Zhou, G. Qian, B. Chen, *Adv. Mater.* **2016**, *28*, 8819.
[8] H. Furukawa, K. E. Cordova, M. O'Keeffe, O. M. Yaghi, *Science* **2013**, *341*, 974.
[9] G. Maurin, C. Serre, A. Cooper, G. Férey, *Chem. Soc. Rev.* **2017**, *46*, 3104.
[10] M. Liu, L. Zhang, M. A. Little, V. Kapil, M. Ceriotti, S. Yang, L. Ding, D. L. Holden, R. Balderas-Xicohténcatl, D. He, R. Clowes, S. Y. Chong, G. Schütz, L. Chen, M. Hirscher, A. I. Cooper, *Science* **2019**, *366*, 613.
[11] A. E. Baumann, D. A. Burns, B. Liu, V. S. Thoi, *Commun Chem* **2019**, *2*, 86.
[12] V. I. Isaeva, L. M. Kustov, in *Zeolites and Zeolite-Like Materials*, Elsevier, New York **2016**, pp. 33–109.
[13] B. Yilmaz, N. Trukhan, U. Müller, *Chin. J. Catal.* **2012**, *33*, 3.
[14] A. I. Cooper, *Nat. Chem.* **2021**, *13*, 620.
[15] M. Simard, D. Su, J. D. Wuest, *J. Am. Chem. Soc.* **1991**, *113*, 4696.
[16] F. A. A. Paz, J. Klinowski, S. M. F. Vilela, J. P. C. Tomé, J. A. S. Cavaleiro, J. Rocha, *Chem. Soc. Rev.* **2012**, *41*, 1088.
[17] G. Zhang, M. Mastalerz, *Chem. Soc. Rev.* **2014**, *43*, 1934.
[18] S. Yuan, L. Feng, K. Wang, J. Pang, M. Bosch, C. Lollar, Y. Sun, J. Qin, X. Yang, P. Zhang, Q. Wang, L. Zou, Y. Zhang, L. Zhang, Y. Fang, J. Li, H. Zhou, *Adv. Mater.* **2018**, *30*, 1704303.
[19] S. Das, P. Heasman, T. Ben, S. Qiu, *Chem. Rev.* **2017**, *117*, 1515.
[20] S. T. Meek, J. A. Greathouse, M. D. Allendorf, *Adv. Mater.* **2011**, *23*, 249.
[21] J. L. C. Rowsell, O. M. Yaghi, *Microporous Mesoporous Mater.* **2004**, *73*, 3.
[22] A. Schneemann, V. Bon, I. Schwedler, I. Senkovska, S. Kaskel, R. A. Fischer, *Chem. Soc. Rev.* **2014**, *43*, 6062.
[23] A. P. Côté, A. I. Benin, N. W. Ockwig, M. O'Keeffe, A. J. Matzger, O. M. Yaghi, *Science* **2005**, *310*, 1166.
[24] S. Kandambeth, K. Dey, R. Banerjee, *J. Am. Chem. Soc.* **2019**, *141*, 1807.
[25] P. J. Waller, F. Gándara, O. M. Yaghi, *Acc. Chem. Res.* **2015**, *48*, 3053.
[26] G. Férey, *Chem. Soc. Rev.* **2008**, *37*, 191.
[27] S. Kitagawa, R. Kitaura, S. Noro, *Angew. Chem., Int. Ed.* **2004**, *43*, 2334.
[28] R. Freund, S. Canossa, S. M. Cohen, W. Yan, H. Deng, V. Guillerm, M. Eddaoudi, D. G. Madden, D. Fairen-Jimenez, H. Lyu, L. K. Macreadie, Z. Ji, Y. Zhang, B. Wang, F. Haase, C. Wöll, O. Zaremba, J. Andreo, S. Wuttke, C. S. Diercks, *Angew. Chem., Int. Ed.* **2021**, *60*, 23946.
[29] T. Tozawa, J. T. A. Jones, S. I. Swamy, S. Jiang, D. J. Adams, S. Shakespeare, R. Clowes, D. Bradshaw, T. Hasell, S. Y. Chong, C. Tang, S. Thompson, J. Parker, A. Trewin, J. Bacsa, A. M. Z. Slawin, A. Steiner, A. I. Cooper, *Nat. Mater.* **2009**, *8*, 973.
[30] T. Hasell, A. I. Cooper, *Nat. Rev. Mater.* **2016**, *1*, 16053.

© 2023 The Authors. Advanced Functional Materials published by Wiley-VCH GmbH

16163028, 2023, 36, Downloaded from https://advanced.onlinelibrary.wiley.com/doi/10.1002/adfm.202302033 by Technische Universitaet Dortmund, Wiley Online Library on [20/01/2025]. See the Terms and Conditions (https://onlinelibrary.wiley.com/terms-and-conditions) on Wiley Online Library for rules of use; OA articles are governed by the applicable Creative Commons License

[31] P. Wagner, F. Rominger, W. S. Zhang, J. H. Gross, S. M. Elbert, R. R. Schröder, M. Mastalerz, *Angew. Chem., Int. Ed.* **2021**, *60*, 8896.
[32] K. Tian, S. M. Elbert, X. Y. Hu, T. Kirschbaum, W. S. Zhang, F. Rominger, R. R. Schröder, M. Mastalerz, *Adv. Mater.* **2022**, *34*, 2202290.
[33] S. Pullen, G. H. Clever, *Acc. Chem. Res.* **2018**, *51*, 3052.
[34] A. J. Gosselin, C. A. Rowland, E. D. Bloch, *Chem. Rev.* **2020**, *120*, 8987.
[35] A. I. Cooper, *ACS Cent. Sci.* **2017**, *3*, 544.
[36] J. R. Holst, A. Trewin, A. I. Cooper, *Nat. Chem.* **2010**, *2*, 915.
[37] Y. Jin, Q. Wang, P. Taynton, W. Zhang, *Acc. Chem. Res.* **2014**, *47*, 1575.
[38] S. Lee, H. Jeong, D. Nam, M. S. Lah, W. Choe, *Chem. Soc. Rev.* **2021**, *50*, 528.
[39] S. Furukawa, N. Horike, M. Kondo, Y. Hijikata, A. Carné-Sánchez, P. Larpent, N. Louvain, S. Diring, H. Sato, R. Matsuda, R. Kawano, S. Kitagawa, *Inorg. Chem.* **2016**, *55*, 10843.
[40] A. Carné-Sánchez, J. Albalad, T. Grancha, I. Imaz, J. Juanhuix, P. Larpent, S. Furukawa, D. Maspoch, *J. Am. Chem. Soc.* **2019**, *141*, 4094.
[41] A. Carné-Sánchez, G. A. Craig, P. Larpent, T. Hirose, M. Higuchi, S. Kitagawa, K. Matsuda, K. Urayama, S. Furukawa, *Nat. Commun.* **2018**, *9*, 2506.
[42] J. Albalad, A. Carné-Sánchez, T. Grancha, L. Hernández-López, D. Maspoch, *Chem. Commun.* **2019**, *55*, 12785.
[43] M. A. Little, A. I. Cooper, *Adv. Funct. Mater.* **2020**, *30*, 1909842.
[44] U. Mueller, M. Schubert, F. Teich, H. Puetter, K. Schierle-Arndt, J. Pastré, *J. Mater. Chem.* **2006**, *16*, 626.
[45] C. Healy, K. M. Patil, B. H. Wilson, L. Hermanspahn, N. C. Harvey-Reid, B. I. Howard, C. Kleinjan, J. Kolien, F. Payet, S. G. Telfer, P. E. Kruger, T. D. Bennett, *Coord. Chem. Rev.* **2020**, *419*, 213388.
[46] J. C. Tan, A. K. Cheetham, *Chem. Soc. Rev.* **2011**, *40*, 1059.
[47] X. S. Zhao, F. Su, Q. Yan, W. Guo, X. Y. Bao, L. Lv, Z. Zhou, *J. Mater. Chem.* **2006**, *16*, 637.
[48] C. H. Görbitz, *Chem. - Eur. J.* **2007**, *13*, 1022.
[49] B. Chen, X. Zeng, U. Baumeister, G. Ungar, C. Tschierske, *Science* **2005**, *307*, 96.
[50] X. Zeng, R. Kieffer, B. Glettner, C. Nürnberger, F. Liu, K. Pelz, M. Prehm, U. Baumeister, H. Hahn, H. Lang, G. A. Gehring, C. H. M. Weber, J. K. Hobbs, C. Tschierske, G. Ungar, *Science* **2011**, *331*, 1302.
[51] S. Henke, A. Schneemann, A. Wütscher, R. A. Fischer, *J. Am. Chem. Soc.* **2012**, *134*, 9464.
[52] R. Pallach, J. Keupp, K. Terlinden, L. Frentzel-Beyme, M. Kloß, A. Machalica, J. Kotschy, S. K. Vasa, P. A. Chater, C. Sternemann, M. T. Wharmby, R. Linser, R. Schmid, S. Henke, *Nature Communications* **2021**, *12*, https://doi.org/10.1038/s41467-021-24188-4.
[53] C. A. Hunter, J. K. M. Sanders, *J. Am. Chem. Soc.* **1990**, *112*, 5525.
[54] C. R. Martinez, B. L. Iverson, *Chem. Sci.* **2012**, *3*, 2191.
[55] J. A. Kaduk, *Acta Crystallogr. B* **2000**, *56*, 474.
[56] D. W. Breck, *Zeolite Molecular Sieves: Structure Chemistry and Use*, John Wiley & Sons Inc., New York **1974**.
[57] L. K. Macreadie, O. T. Qazvini, R. Babarao, *ACS Appl. Mater. Interfaces* **2021**, *13*, 30885.
[58] C.-A. Tao, J.-F. Wang, *Crystals (Basel)* **2020**, *11*, 15.
[59] P. Vervoorts, J. Stebani, A. S. J. Méndez, G. Kieslich, *ACS Mater. Lett.* **2021**, *3*, 1635.
[60] J. Chu, F.-S. Ke, Y. Wang, X. Feng, W. Chen, X. Ai, H. Yang, Y. Cao, *Commun Chem* **2020**, *3*, 5.
[61] A. Knebel, A. Bavykina, S. J. Datta, L. Sundermann, L. Garzon-Tovar, Y. Lebedev, S. Durini, R. Ahmad, S. M. Kozlov, G. Shterk, M. Karunakaran, I. D. Carja, D. Simic, I. Weilert, M. Klüppel, U. Giese, L. Cavallo, M. Rueping, M. Eddaoudi, J. Caro, J. Gascon, *Nat. Mater.* **2020**, *19*, 1346.
[62] H. Yuan, G. Liu, Z. Qiao, N. Li, P. J. S. Buenconsejo, S. Xi, A. Karmakar, M. Li, H. Cai, S. J. Pennycook, D. Zhao, *Adv. Mater.* **2021**, *33*, 2101257.

© 2023 The Authors. Advanced Functional Materials published by Wiley-VCH GmbH

16163028, 2023, 36, Downloaded from https://advanced.onlinelibrary.wiley.com/doi/10.1002/adfm.202302033 by Technische Universitaet Dortmund, Wiley Online Library on [20/01/2025]. See the Terms and Conditions (https://onlinelibrary.wiley.com/terms-and-conditions) on Wiley Online Library for rules of use; OA articles are governed by the applicable Creative Commons License